Oceanologia (2020) 62, 309—325

Available online at www.sciencedirect.com

ScienceDirect

journal homepage: www.journals.elsevier.com/oceanologia

ORIGINAL RESEARCH ARTICLE

The demand analysis of oceanic T-S-V 3D reconstruction on wide-swath SSH data features based on ROMS and 4DVAR

Chaojie Zhou[1,*], **Jie Zhang**[1,2], **Jungang Yang**[2], **Lei Cao**[3]

[1] *China University of Petroleum, College of Oceanography and Space Informatics, Qingdao, China*
[2] *First Institute of Oceanography, Ministry of Natural Resources, Qingdao, China*
[3] *Beijing Research Institute of Telemetry, Beijing, China*

Received 13 June 2019; accepted 27 February 2020
Available online 13 March 2020

KEYWORDS
3D Ocean state estimation;
Wide-swath altimeter;
Accuracy;
Spatial-temporal resolution

Summary Future wide-swath altimetry missions will provide high-resolution information about ocean surface elevation, and facilitate the characterization of meso- and sub-mesoscale ocean activities. In this study, the demand analysis of three-dimensional (3D) oceanic state reconstruction on wide-swath SSH data features was evaluated using a data assimilation strategy. Three groups of experiments were performed to determine if the wide-swath altimetry observations would improve the three-dimensional (3D) field estimates of ocean temperature-salinity-velocity (T-S-V), and to evaluate how the spatial and temporal resolution and accuracy of the wide-swath altimetry observations affected the ocean state estimation. The Regional Ocean Modeling System and the four-dimensional variational data assimilation method were used in the experiments, with numerical simulation for the Taiwan region at a resolution of 1/10° as the example. The sensitivity of the 3D ocean state construction to the wide-swath altimetry measurements was also investigated. The results showed that the wide-swath sea surface height (SSH) measurements would have an overall positive impact on the 3D T-S-V field and that the positive effect would increase as the resolution and accuracy of the observations increased, but the net benefits would gradually decrease. Among the three examined features

* Corresponding author at: China University of Petroleum, College of Oceanography and Space Informatics, Qingdao 266580, China.
E-mail address: hitzcj@163.com (C. Zhou).
Peer review under the responsibility of the Institute of Oceanology of the Polish Academy of Sciences.

Production and hosting by Elsevier

https://doi.org/10.1016/j.oceano.2020.02.004

of the wide-swath altimetry observations, the temporal resolution had the most influence on the 3D ocean state analysis.

1. Introduction

Since 1973, many altimetry missions, such as Skylab, Geosat, ERS, Topex/Poseidon, and the Jason surveys, have been launched to measure sea surface elevation. Information about sea surface height (SSH) collected by altimeters has become an essential element of ocean investigations (Gaspar et al., 1994; Hwang et al., 1998; Martin-Neira et al., 1998; Qiu and Chen, 2005; Tandeo et al., 2014). Altimetry observations can be merged with other data to give the broadest possible interpretation of the mechanisms that drive oceanic processes (Morrow and Birol, 1998; Piecuch and Ponte, 2011; Soto-Mardones et al., 2004; Wang and Liu 2006), and may also be assimilated into ocean and climate models to enhance the accuracy of the predictions (Cooper and Haines, 1996; De Mey and Robinson, 1987; Evensen and Van Leeuwen, 1996; Matsumoto et al., 2000; Mellor and Ezer, 1991). While the resolution and accuracy of the altimetry data are the most important aspects of these modelling applications, to date, few researchers have presented the detailed demand for SSH observations in ocean analysis.

Thanks to these continuous worldwide observations of SSH from satellite altimeters, we have been able to extend our research in various directions and, for example, gain knowledge about the variations in absolute circulation (Chelton et al., 1990; Korotaev et al., 2003; Miller et al., 1988; Nerem et al., 1990; Strub and James, 2002), and map eddies at the global scale (Chaigneau et al., 2008; Le Traon et al., 1990; Traon, 1991; Wang et al., 2003). Generally, ocean circulation occurs at the large-scale (ocean-basin scale) and could be recognized from the altimetry observations easily. Mesoscale eddies have a horizontal scale of between 25 and 500 km and generally move across the ocean at speeds of less than 10 km/day (Koblinsky et al., 1992). However, the sub-mesoscale processes (with scales between 50 and 100 km) are not visible in the images from a traditional altimeter (Klein et al., 2015). It is expected that the future wide-swath altimetry, such as the Surface Water and Ocean Topography (SWOT) mission (to be launched in 2021), would provide the ocean SSH fields in two dimensions at a global scale and make a prominent contribution to the study of sub-mesoscale processes (Bell et al., 2015; Le Traon et al., 2017).

Moreover, the sea surface elevation reflects more than just the surface conditions, and may also benefit for the estimates of three-dimensional (3D) ocean state in ocean modelling system. In some of the previous studies, surface elevation information has been proved to have a positive impact on the ocean model (Fan et al., 2004; Killworth et al., 2001; Kurapov et al., 2011; Martin et al., 2007; Penduff et al., 2002). Conversely, the major challenge for altimetry in the future is how to incorporate data from both wide-swath and conventional along-track altimeters into high-resolution ocean general circulation models, to facilitate a detailed description and high-resolution forecast of the ocean state (Pujol et al., 2012). Approaching the challenge of using wide-swath altimetry data, Gaultier et al. (2016) underline the need to test their effective impact on ocean analyses and forecasts by performing observing system simulation experiments. Using the simulated observations derived from a fully eddy-resolving free simulation, the contribution of forthcoming wide-swath altimetry missions on the ocean analysis and forecasting system is firstly quantified (Bonaduce et al., 2018).

To further clarify the demand of 3D ocean state estimations on the wide-swath altimetry data, the impact of SSH assimilations was evaluated at various spatial and temporal resolutions and levels of accuracy in this study (Figure 1). The paper is organized as follows. The method for simulating the wide-swath altimetry observations is described in Section 2. Section 3 refers to the main body of the paper, in which we discuss how the future wide-swath SSH observations will influence data assimilation based on the Regional Ocean Modeling System (ROMS) and four-dimensional variational data assimilation (4DVAR). In section 4, the sensitivity analysis of 3D ocean state simulation to the wide-swath SSH

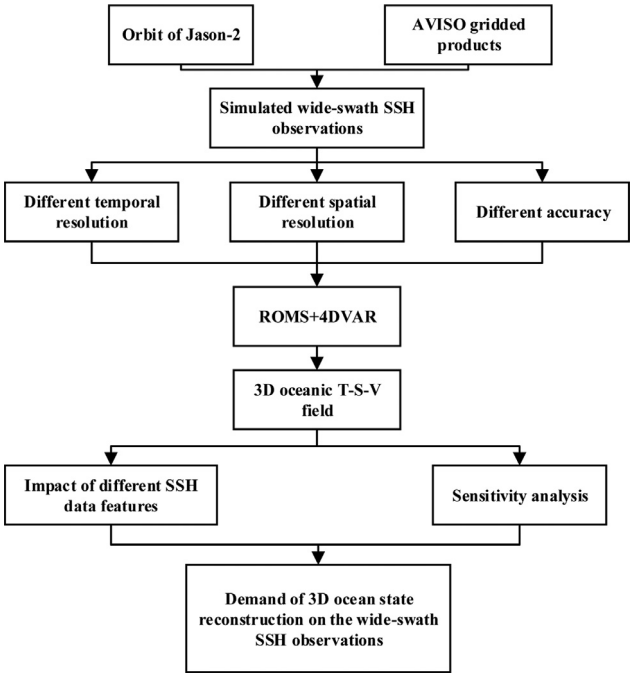

Figure 1 Flowchart of the demand analysis of 3D ocean state on the wide-swath altimeter observations.

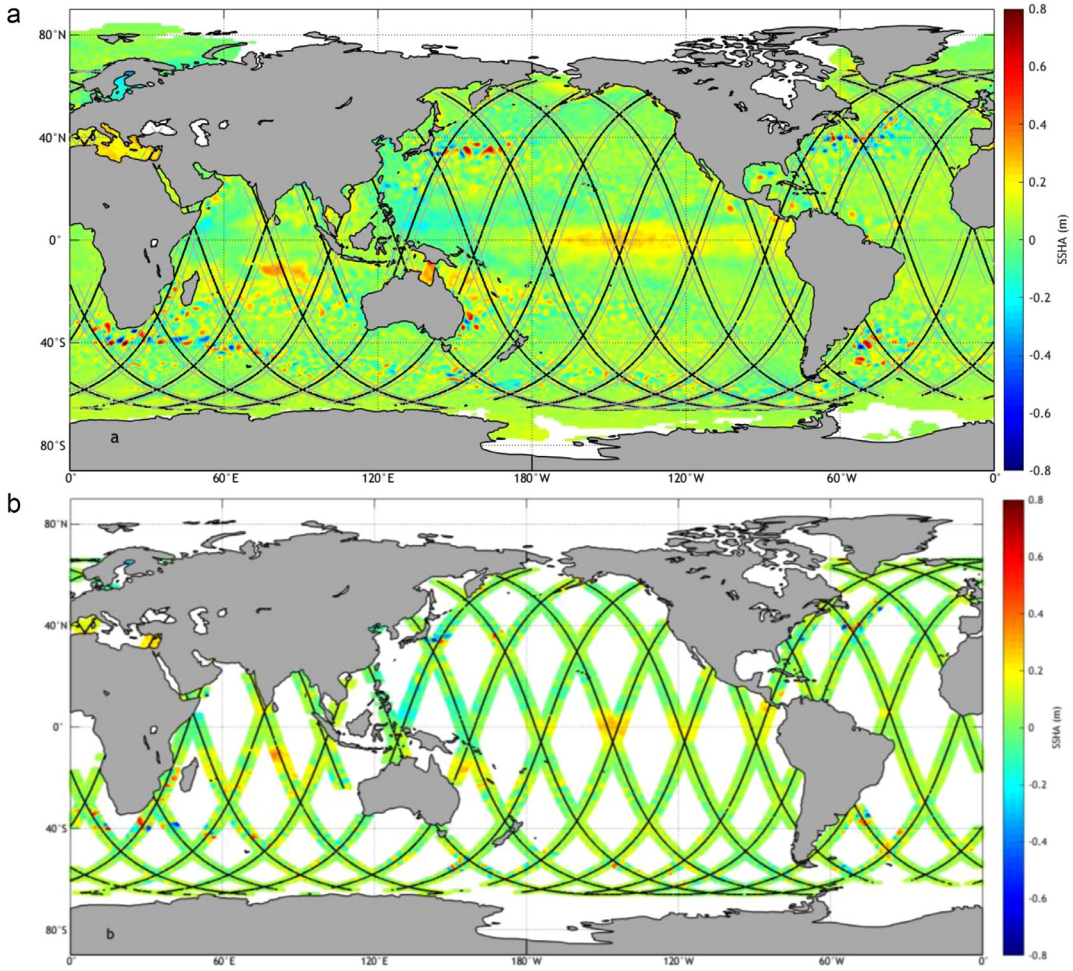

Figure 2 Graph a) is the global sea surface height anomaly (SSHA) from AVISO and the observation orbit of Jason-2 (black lines) on 1 January 2010. The gray lines are the two boundaries of the simulated altimeter's swath, derived by translating the measurements of Jason-2 horizontally. Graph b) presents the simulated altimeter observations with a 6°-wide swath, and the Jason-2 orbit (black lines).

observations, carried out to further validate the conclusion from section 3, are considered. Section 5 comprises a summary and discussion.

2. Simulation of the wide-swath altimetry observations

The wide-swath altimetry observations were extracted from the AVISO gridded products (SEALEVEL_GLO_PHY_L4_REP_OBSERVATIONS_008_047 available at http://marine.cop-ernicus.eu/) based on the Jason-2 orbit (see Figure 2). The details of the wide-swath altimetry simulation are presented as follows.

According to previous studies (Ducet et al., 2000; Vélez-Belchí et al., 2013), some detailed characteristics of ocean state could be reconstructed in the gridded SSH products (as shown in Figure 1). To simulate the future altimeter of a certain swath, the measure orbit of Jason-2 were employed and translated horizontally with a desired swath width W. Namely, the zonal boundary of simulated wide-swath orbit was restricted by the longitude of Jason-2 measurements (Lon) and the swath W, and the SSH data located in [Lon-W/2, Lon+W/2] were extracted from the AVISO gridded products.

The wide-swath altimetry observations using a 6° swath are presented in Figure 1(b). Unfortunately, the extracted SSH measurements were very limited, and we may not find any observations in the study region. Therefore, a track union during the repeat period of Jason-2 (9.9156 days) was considered as the hypothetical orbit of wide-swath altimeter, so that we could make a reasonable coverage for the regional simulation. The 10d and 5d union of observations generated from 1 Jan 2010 to 10 Jan 2010 near Taiwan Island are presented in Figure 3. Here, the 5d union was selected every two days. As shown in Figure 3, the data of both alternatives were sufficiently dense to cover the whole region, but the gaps between the two adjacent orbits of 10d union were too narrow (~3°) to specify a wide-swath. Thus, in this study, the 5d union choice was adopted to simulate the wide-swath altimetry observations, and the extracted observations are presented in Figure 3(c).

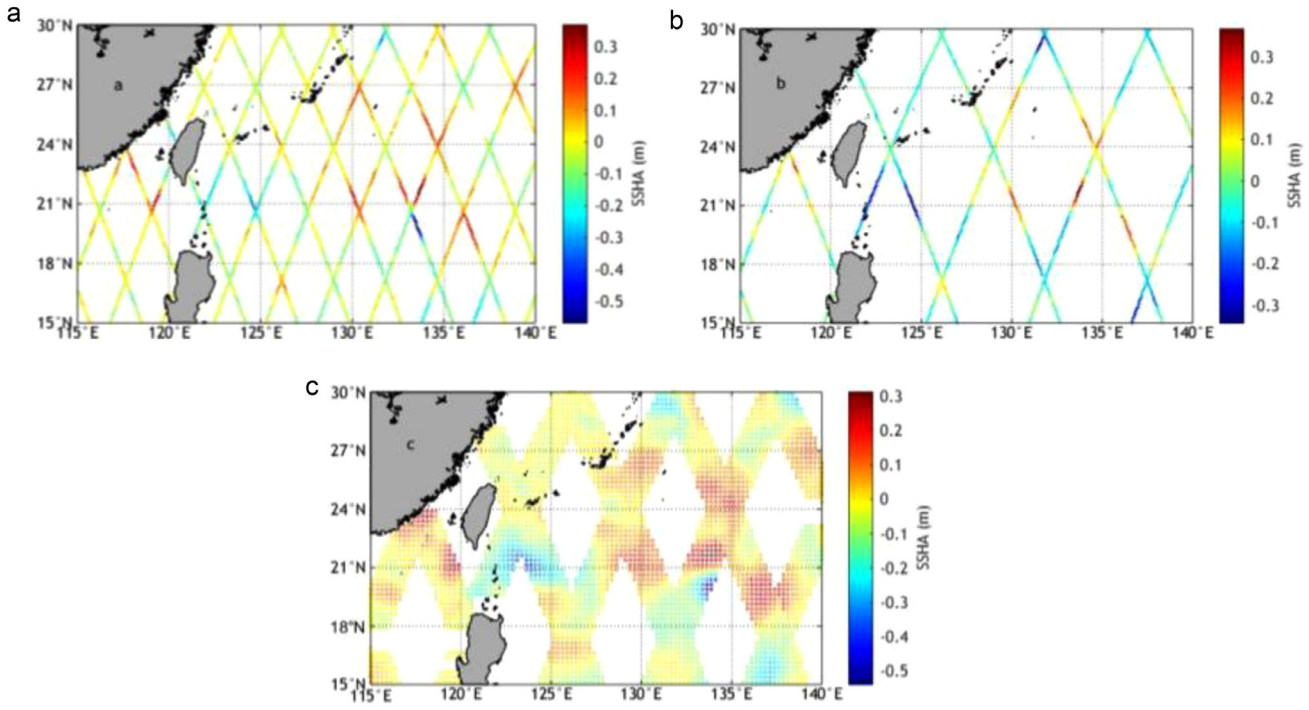

Figure 3 Graph a) and b) are the 10d and 5d orbit simulations based on the Jason-2 measurements. Graph c) represents the simulated altimetry observations with a 2°-wide swath near Taiwan Island.

3. Impact of wide-swath SSH observations on the 3D T-S-V estimates

In section 2, the simulation of wide-swath altimetry observations was performed. In the following, three groups of experiments were carried out with ROMS and 4DVAR, to explore how sensitive the oceanic 3D T-S-V estimates are to the features of the wide-swath SSH data, including the spatial and temporal resolution and accuracy. The configuration of the model and the assimilation were presented at first, and then the impact of the SSH assimilation with different data features is evaluated, respectively.

3.1. Configuration of the model and assimilation

The ocean model ROMS and the 4DVAR scheme were used in the experiments. ROMS is a free-surface, hydrostatic, primitive equation model discretized with a terrain-following vertical coordinate system (Shchepetkin and Mcwilliams, 2005). The model domain covered the area from 15°N to 30°N, and from 115°E to 140°E (Figure 4), with an eddy-resolved horizontal resolution of 0.1° × 0.1° and 30 S-coordinate layers in the vertical. The level 2.5 Mellor Yamada scheme (Mellor and Yamada, 1982) was used to parameterize the vertical mixing process. The temperature and salinity fields were initialized by the Levitus climatology dataset, and the free surface and velocity were set to 0. The bathymetry field was produced from ETOPO1 data (Amante and Eakins, 2009). The minimum and maximum depths across the whole domain were set at 10 and 5000 m, respectively. A daily mean wind field from the Cross-Calibrated

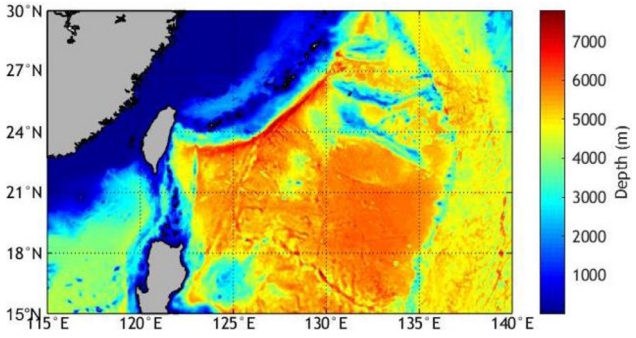

Figure 4 Model domain and bathymetry (m).

Multi-Platform (CCMP) ocean surface wind product (Atlas et al., 2011) with a horizontal resolution of 0.25° × 0.25° was used for the wind field. The other daily atmospheric forcing fields, including heat fluxes, solar radiation fluxes, evaporation-precipitation (E-P), air temperature, and specific humidity, were obtained from the U.S. National Centers of Environmental Prediction (NCEP) reanalysis (Kalnay et al., 1996) at a horizontal resolution of 1.875° × 1.875°. The monthly temperature, salinity, sea surface height, and velocity field from simple ocean data assimilation (SODA) were used for the lateral boundary conditions.

Data for 5 years, starting from 1 Jan. 2005, were integrated into the forward model so that a dynamically balanced state was achieved, and then the outcomes were used to calculate the background error covariance matrix. The parameters that were used to model the background error covariance matrix (D) and the observation error covariance

Table 1 Summary of the SSH assimilation cases at different spatial resolutions.

	Case 1	Case 2	Case 3	Case 4	Case 5
SSH	0.25° × 0.25° gridded products	No SSH	0.25° × 0.25° along-track	0.5° × 0.5° along-track	1° × 1° along-track

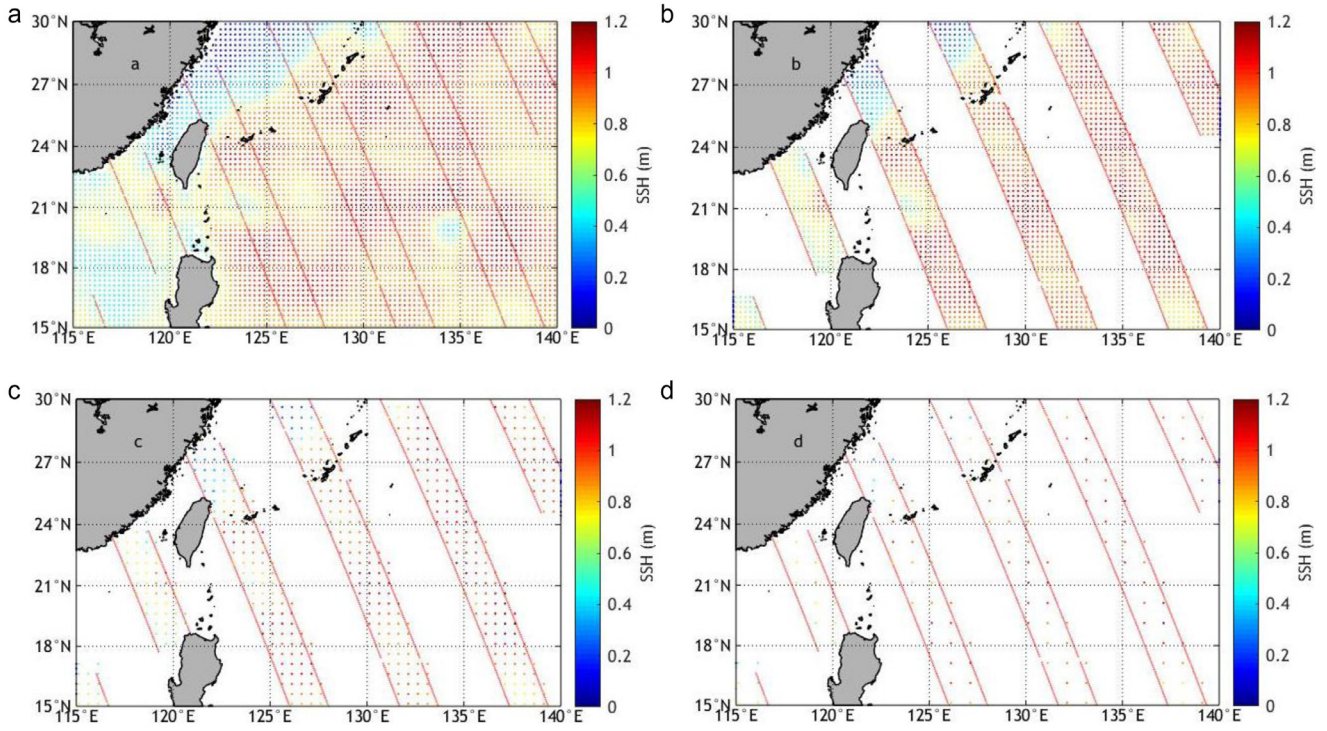

Figure 5 Wide-swath SSH observations at different spatial resolutions (a: AVISO gridded products; b: 0.25° × 0.25°; c: 0.5° × 0.5°; d: 1° × 1°). The boundary (red dotted line) is determined by the orbit of Jason-2 using a 2° swath width.

matrix (R) were designed as Moore et al. (2011). The background errors of all initial conditions control variable components of D were 50 km in the horizontal and 30 m in the vertical. Horizontal correlation scales chosen for the background surface forcing error components of D were 300 km for wind stress and 100 km for heat and freshwater fluxes. The correlation lengths for the background open boundary condition error components of D were chosen to be 100 km in the horizontal and 30 m in the vertical. The observation errors were assumed to be uncorrelated in space and time, and the variances along the main diagonal of R were assigned as a combination of the measurement error and the error of representativeness, which are generally additive. A measurement error of 0.02 m was chosen for AVISO SSH.

3.2. Impact of SSH at different spatial resolutions

An experiment with five cases was designed to evaluate the impact of the spatial resolution on the 3D ocean T-S-V field. The details are listed in Table 1. In case 1, the 0.25° × 0.25° gridded SSH observations were assimilated and its outcomes were regarded as the ideal scenario. Due to the verified positive impact of the SSH measurements of our previous study (Zhou et al., 2018), the outcome of case 1 was sufficiently accurate to assess the other cases. In cases 3–5, the SSH observations with different spatial resolutions were generated by choosing alternately along the satellite track, and the derived observations were assimilated, respectively. To highlight the effect of SSH assimilation, case 2 with no data assimilation was also performed.

In the following, the model outputs of case 1 were denoted as $T(x, y, z, t)$ and the results of the comparative cases were $M_i(x, y, z, t)$ where $i=2, 3, \cdots$. Moreover, the temporally and vertically averaged error $H_i(x, y)$, the temporally and horizontally averaged error $V_i(z)$, and the spatially averaged error $S_i(t)$ were calculated as:

$$H_i(x,y) = \frac{1}{l_z l_t} \sum_z \sum_t |M_i(x,y,z,t) - T(x,y,z,t)|,$$

$$V_i(z) = \frac{1}{l_x l_y l_t} \sum_x \sum_y \sum_t |M_i(x,y,z,t) - T(x,y,z,t)|,$$

$$S_i(t) = \frac{1}{l_x l_y l_z} \sum_x \sum_y \sum_z |M_i(x,y,z,t) - T(x,y,z,t)|,$$

where l_x, l_y, l_z, and l_t were the dimensions of the four-dimensional model results, respectively.

For simplicity, only the observations of the ascending orbit were employed. The re-formed wide-swath SSH observations at different spatial resolutions are shown in Figure 5. As we can see, the extracted observations only

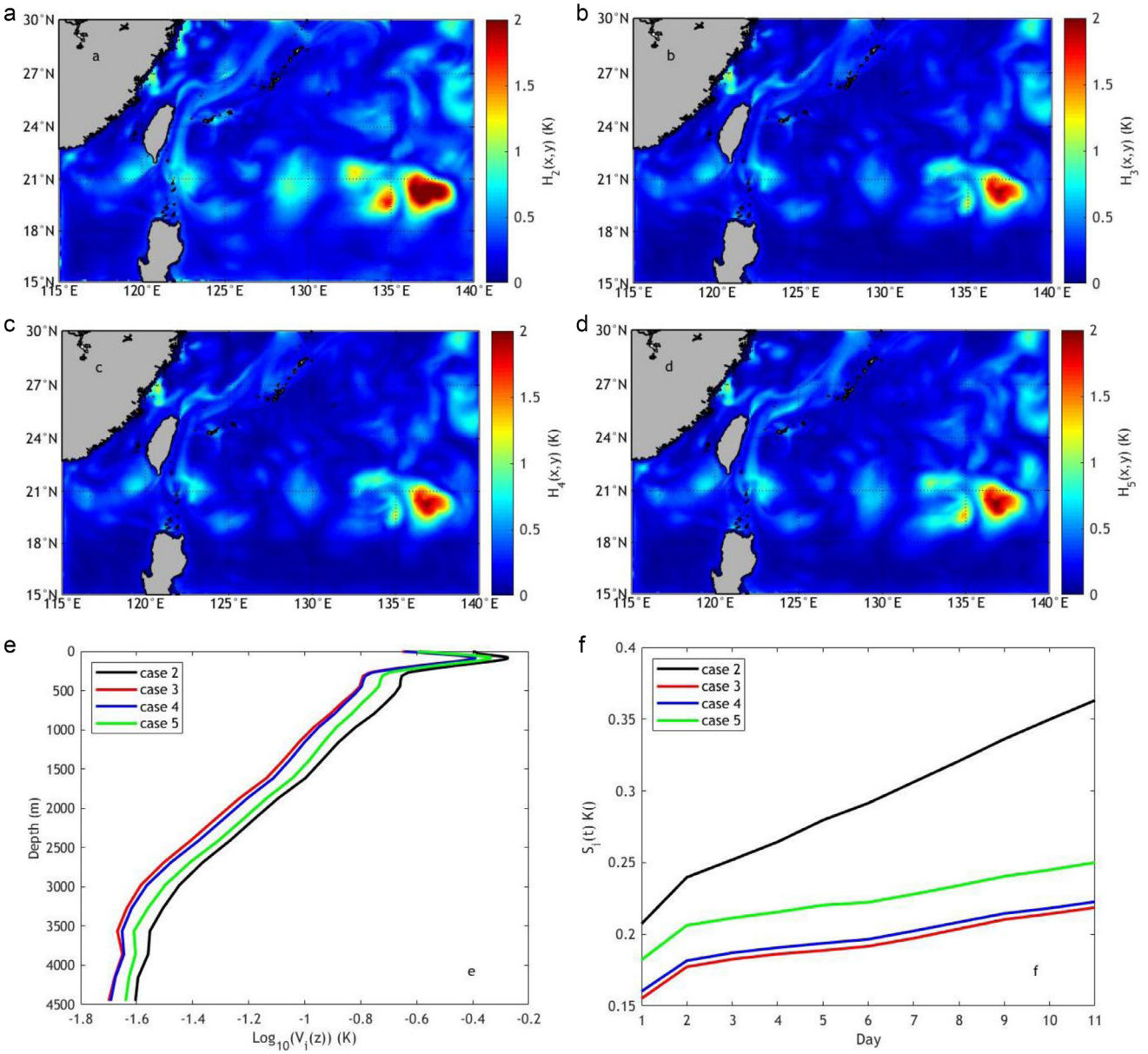

Figure 6 Evaluation of the temperature outcomes of SSH assimilation cases at different spatial resolutions. Here, graphs a)–d) is the temporal and vertical averaged error $H_i(x,y)$ (i=2, 3, 4, 5) of the 3D temperature field for cases 2–5. Otherwise, graphs e) and f), each presents the temporal and horizontal averaged error $V_i(z)$ and spatial averaged error $S_i(t)$, in which lines with different color give the results of cases 2–5, respectively.

reflected the local sea level elevation characteristics, and the amount of information contained in the along-track observations varied with the spatial resolution. This suggested that the positive enhancement may decrease considerably if the wide-swath observations became locally sparse.

As shown earlier, the outcomes of case 1 were used as the true states to verify the 3D T-S-V fields derived in cases 2–5. The spatial and temporal errors associated with the 3D temperature field are illustrated in Figure 6. As shown in Figure 6, the accuracy enhancement increased as the spatial resolution increased, but with limited net promotion. Compared with case 2, the outcomes of the remaining cases were obviously enhanced, and the enhancement of case 3 was the greatest, in which the 0.25° × 0.25° along-track observations were assimilated. Besides, the spatially averaged error tended to increase as the model ran forward, mainly caused by the accumulation of gaps between the ideal gridded and simulated along-track observations.

Meanwhile, the 3D salinity and velocity fields were validated. The error statistics results are presented in Figure 7 and Figure 8, and some similar conclusion was obtained. But the salinity and velocity estimations showed a different sensitivity to the spatial resolution of wide-swath SSH observations. As we can see from Figures 6–8, the temperature

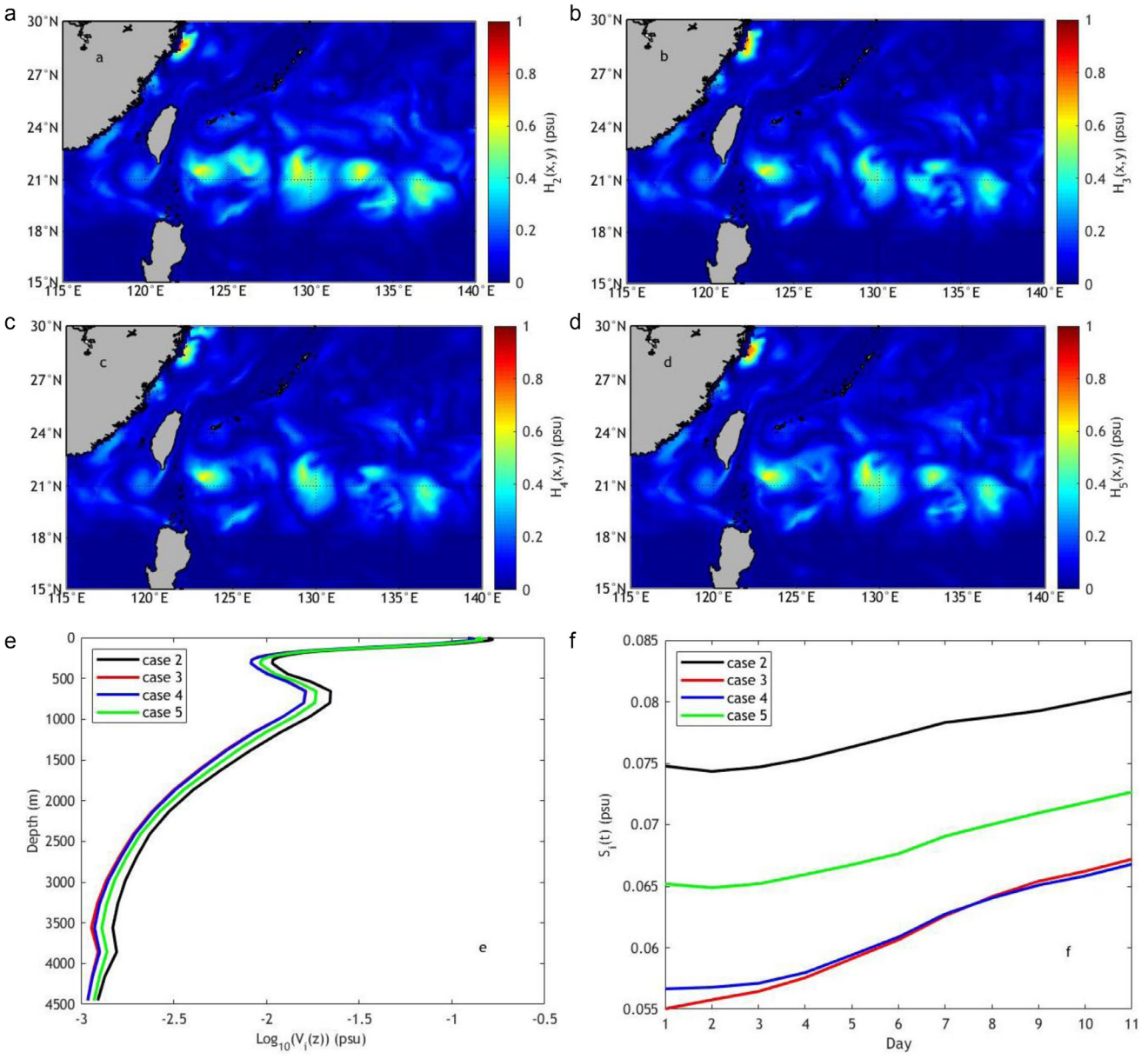

Figure 7 Evaluation of the salinity outcomes of SSH assimilation cases at different spatial resolutions. Graphs a)—f) are presented similarly as Figure 6, but for the 3D salinity field.

estimation was enhanced by a maximum of 0.15°C, but for the salinity and velocity field, the values were 0.02 psu and 0.01 m/s, respectively.

3.3. Impact of SSH at different temporal resolutions

In this section, an experiment with five cases was carried out using different assimilation intervals, to simulate the situation of SSH observations at different temporal resolutions. The daily AVISO SSH gridded products was adopted as the ideal case, and the reduced intervals every 3, 5, or 10 days were considered, respectively (Table 2). As the higher assimilation frequency are more beneficial for ocean analysis (Powell et al., 2008), the daily assimilation case (case 1) was applied to verify the outcomes of the remaining cases.

Table 2 Summary of the SSH assimilation cases at different intervals.

	Case 1	Case 2	Case 3	Case 4	Case 5
Interval	1-day	No SSH	3-day	5-day	10-day

The evaluation was conducted using the similar strategy in section 3.2, and the results are presented in Figure 9—11. As we can see, the 3D T-S-V field estimated by the 3-day assimilation interval (case 3) presents to be the most accurate scenario. Unlike the accuracy promotion caused by

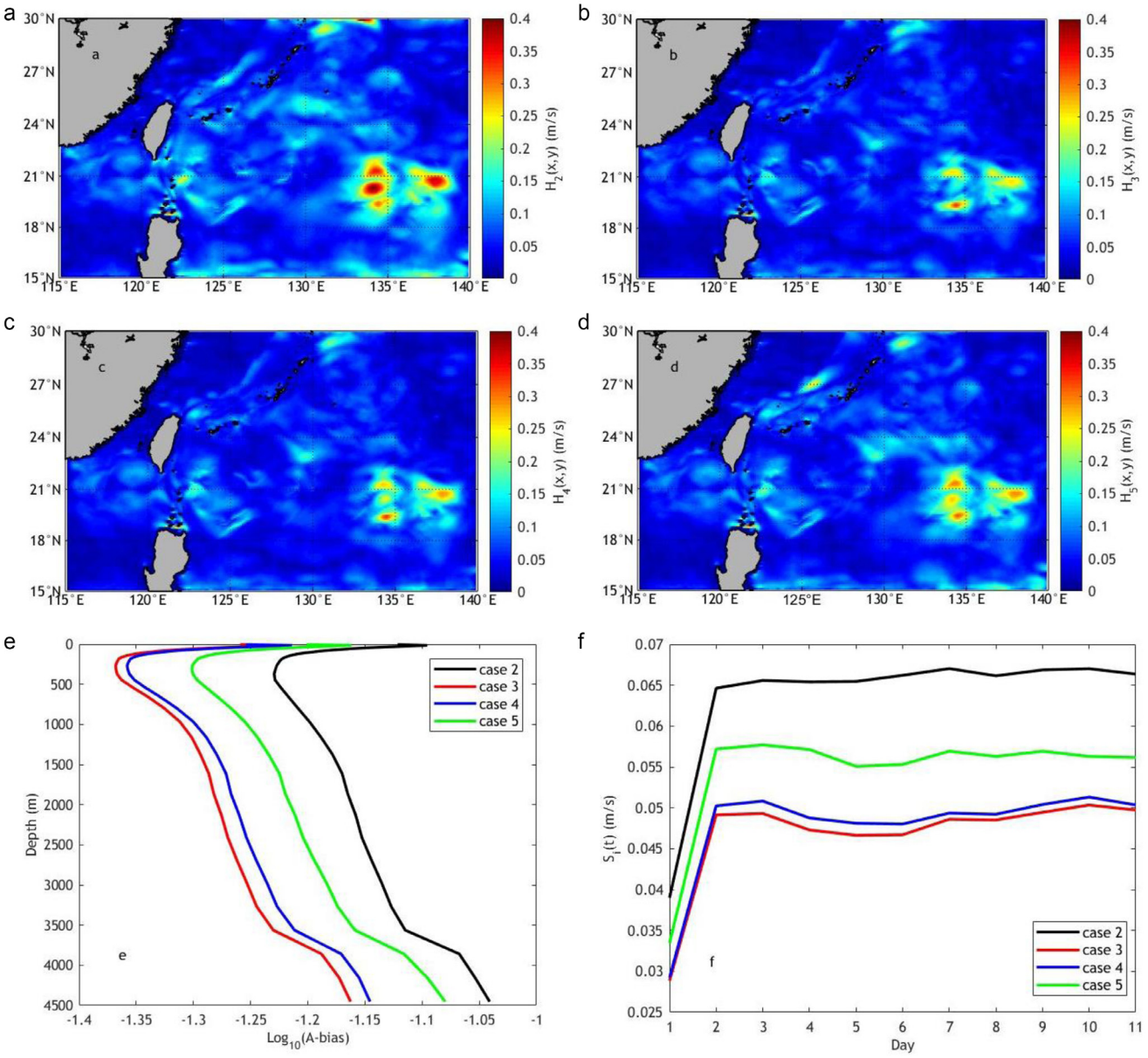

Figure 8 Evaluation of the velocity (eastward component) outcomes of SSH assimilation cases at different spatial resolutions. Graphs a)–f) are presented similarly as Figure 6, but for the 3D velocity field.

the increasement of spatial resolution, more sensitive response was found when the temporal resolution changed. In other words, the temporal resolution of wide-swath altimeter observations seems to be more effective than its spatial features in the data assimilation.

3.4. Impact of SSH at different levels of accuracy

The quality of the observations has an extremely significant role in the data assimilation, and the model solution would be distorted by the inaccurate information. To analyze the impact of the accuracy of wide-swath SSH observations on the 3D T-S-V field construction, some random noise with a fixed mean value was added to the SSH observations. The mean value of added noise was configured as 0.01 m, 0.03 m, 0.05 m, 0.1 m, and 0.15 m. Then the processed SSH observations at different levels of accuracy were assimilated into the ocean model, respectively. The details of the experiment are shown in Table 3, and the assimilation of SSH observations without any noise was taken as the ideal scenario to verify the remaining cases.

The evaluation of 3D T-S-V fields is presented in Figure 12–14. As we can see, the 3D T-S-V simulations were enhanced when the SSH observations were assimilated. However, accuracy of the SSH observations seemed to have less impact than the spatial and temporal resolution, as the difference between cases 3–7 was relatively finite. As shown in Figure 12(h), 13(h), and 14(h), the 3D T-S-V estimations from 0.15 m to 0.01 m were enhanced by less than 0.1°C, 0.05 psu, and 0.03 m/s, respectively. Considering the

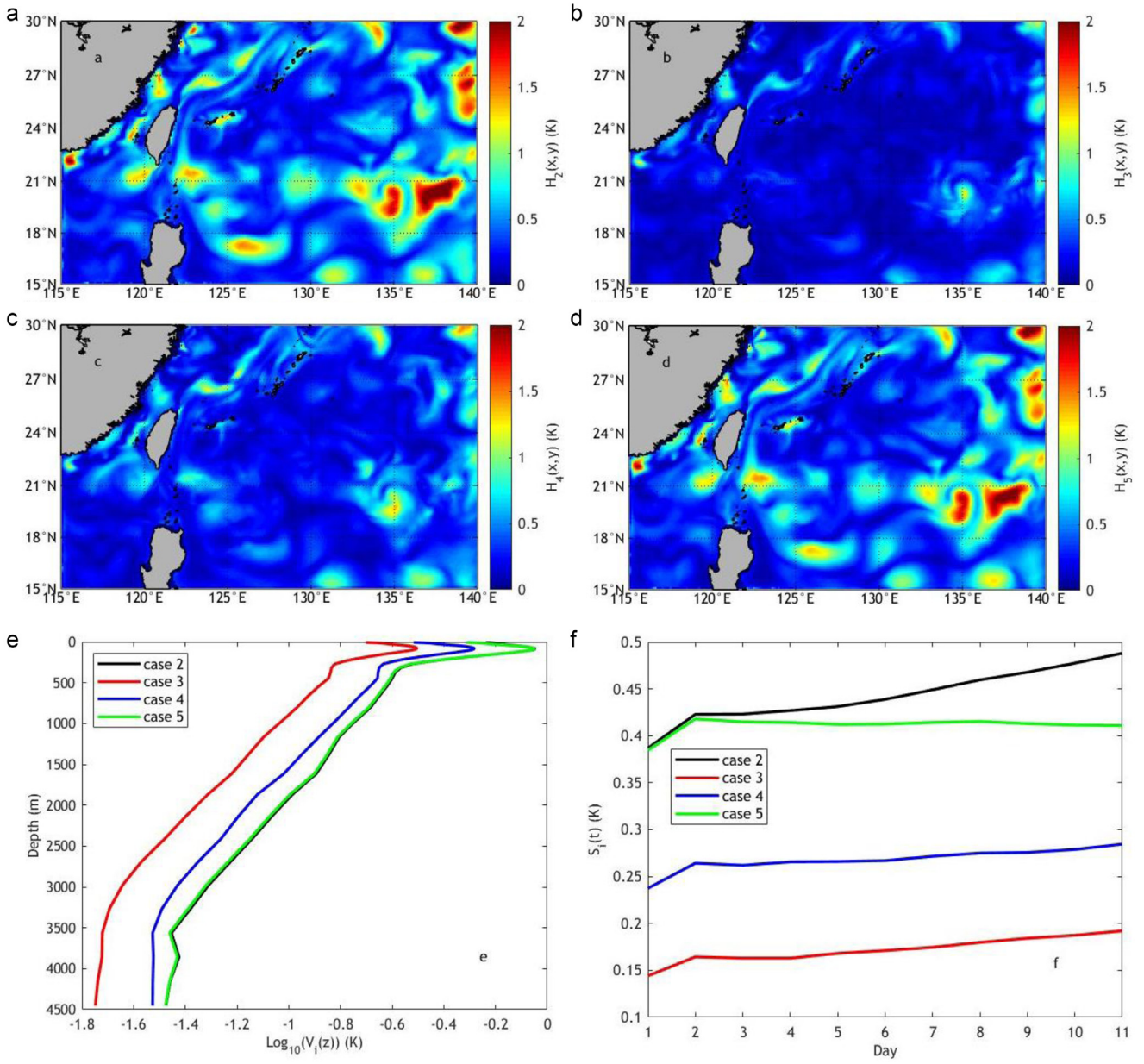

Figure 9 Evaluation of the temperature outcomes of SSH assimilation cases at different temporal resolutions. Here, graphs a)—d), each presents the temporal and vertical averaged error $H_i(x,y)$ (i=2, 3, 4, 5) of the 3D temperature field for cases 2—5. Otherwise, graph e) and f) present the temporal and horizontal averaged error $V_i(z)$ and spatial averaged error $S_i(t)$, in which lines with different color give the results of cases 2—5, respectively.

Table 3 Summary of SSH assimilation cases with different noise levels

	Case 1	Case 2	Case 3	Case 4	Case 5	Case 6	Case 7
SSH	0	No SSH assimilation	0.01 m	0.03 m	0.05 m	0.1 m	0.15 m

addition way of the noise, the abnormal conclusion could be explicated to some degree. The artificial noise was generated with a fixed mean value, which may lead to a similar pattern of the generated observations, and then the characteristics of the sea surface elevation were still contained, more or less.

4. Sensitivity analysis

The above analysis indicated that the 3D T-S-V field estimations could get improved when the wide-swath altimetry observations were assimilated. Among the three discussed features, the temporal resolution was considered to be the

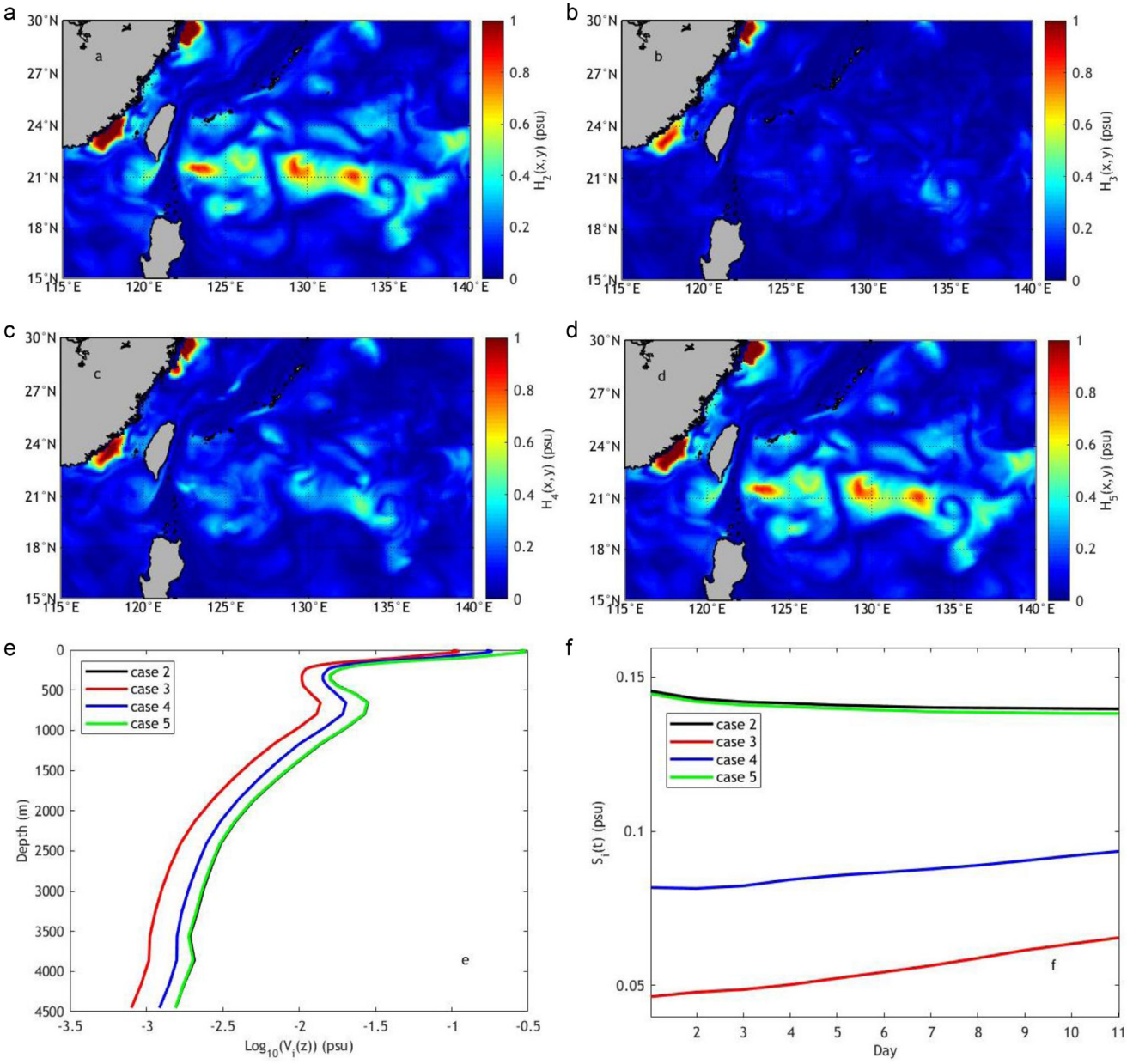

Figure 10 Evaluation of the salinity outcomes of SSH assimilation cases at different temporal resolutions. Graphs a)—f), each presents errors similarly as Figure 9, but for the 3D salinity field.

Table 4 Average absolute bias and the percentage enhancement (in brackets) of the assimilation cases at different spatial resolutions (Sres).

Sres	0.25°	0.5°	1°	No SSH
T (°C)	0.193 (34%)	0.198 (32%)	0.223 (24%)	0.292
S (psu)	0.06 (22%)	0.061 (21%)	0.068 (12%)	0.077
V (m/s)	0.047 (27%)	0.048 (25%)	0.054 (16%)	0.064

Table 5 Average absolute bias and the percentage enhancement (in brackets) of the assimilation cases at different temporal resolutions (Tres).

Tres	3-day	5-day	10-day	No SSH
T (°C)	0.172 (61%)	0.268 (40%)	0.411 (7%)	0.443
S (psu)	0.055 (61%)	0.087 (38%)	0.14 (7%)	0.141
V (m/s)	0.043 (50%)	0.063 (27%)	0.085 (1.2%)	0.086

most effective one. In this section, we tried to quantify the impact of the spatial and temporal resolution and the accuracy, and analyze the sensitivity of 3D T-S-V construction to these wide-swath SSH features.

Comparing with the corresponding ideal scenario cases, the absolute bias of the three groups of experiments was averaged and presented in Table 4—6. Besides, the percentage of enhancement was also calculated with respect to the

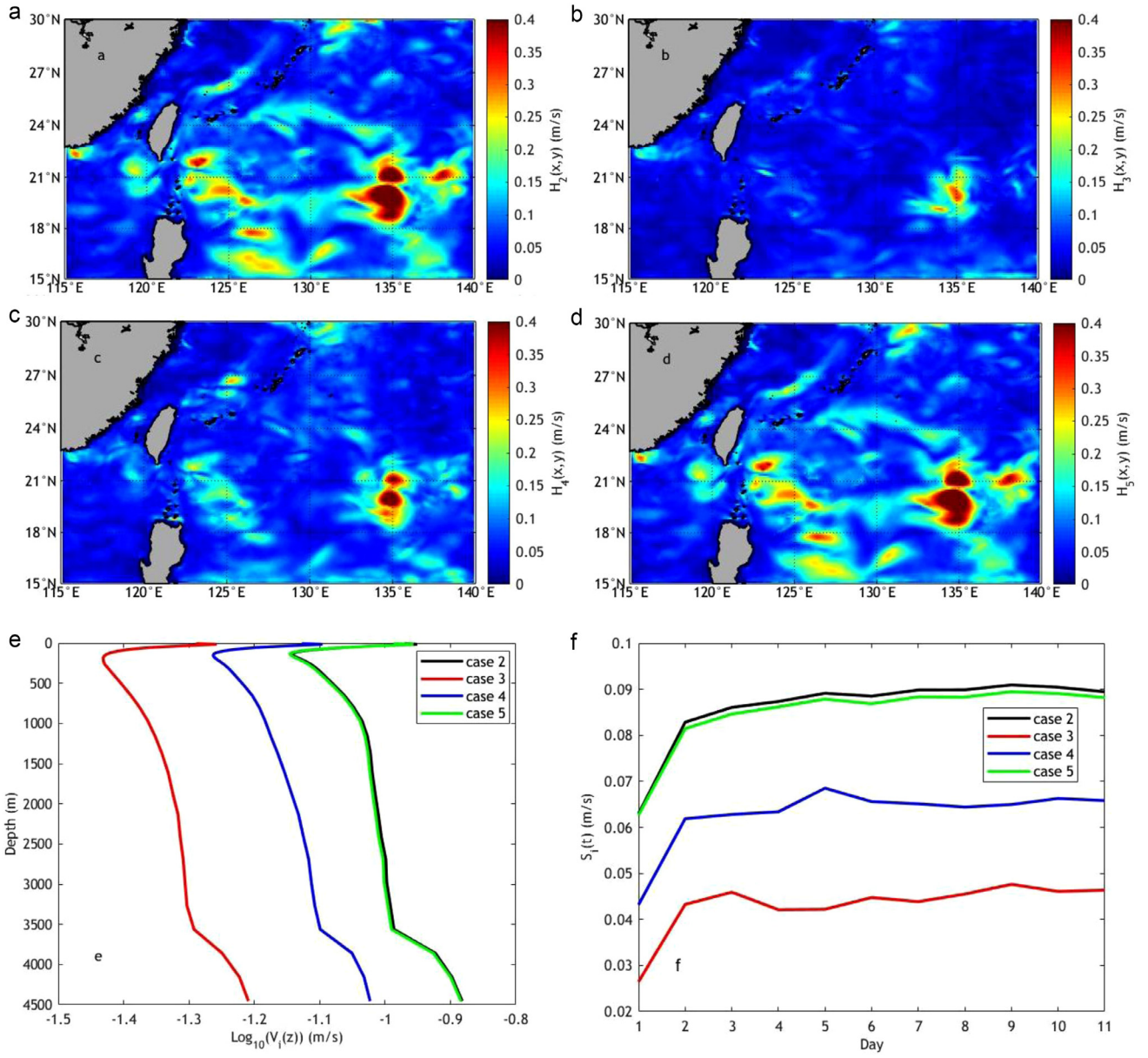

Figure 11 Evaluation of the velocity (eastward component) outcomes of SSH assimilation cases at different temporal resolutions. Graphs a)–f), each presents errors similarly as Figure 9, but for the 3D velocity field.

Table 6 Average absolute bias and the percentage enhancement (in brackets) of the assimilation cases at different accuracy levels.

Accuracy	0.01 m	0.03 m	0.05 m	0.1 m	0.15 m	No SSH
T (°C)	0.009 (98%)	0.021 (95%)	0.034 (92%)	0.074 (83%)	0.106 (76%)	0.441
S (psu)	0.003 (98%)	0.006 (96%)	0.009 (94%)	0.021 (86%)	0.032 (78%)	0.147
V (m/s)	0.002 (98%)	0.005 (94%)	0.009 (89%)	0.018 (79%)	0.025 (70%)	0.084

case without data assimilation. In each group, the positive effect of the SSH assimilation increases with better parameter choices. Moreover, the 3D T-S-V fields showed different sensitivity to these three features, and the temporal resolution of the assimilated wide-swath SSH observations seems to be the most attractive one. As shown in Table 5, the enhancement between two adjacent cases differs by as much as 33%, larger than the variations in Tables 4 and 6.

To make the three groups of experiments comparable, the error scales were normalized accordingly. Firstly, the error of cases without SSH data assimilation and the ideal scenarios were configured as the two extreme values, 1 and

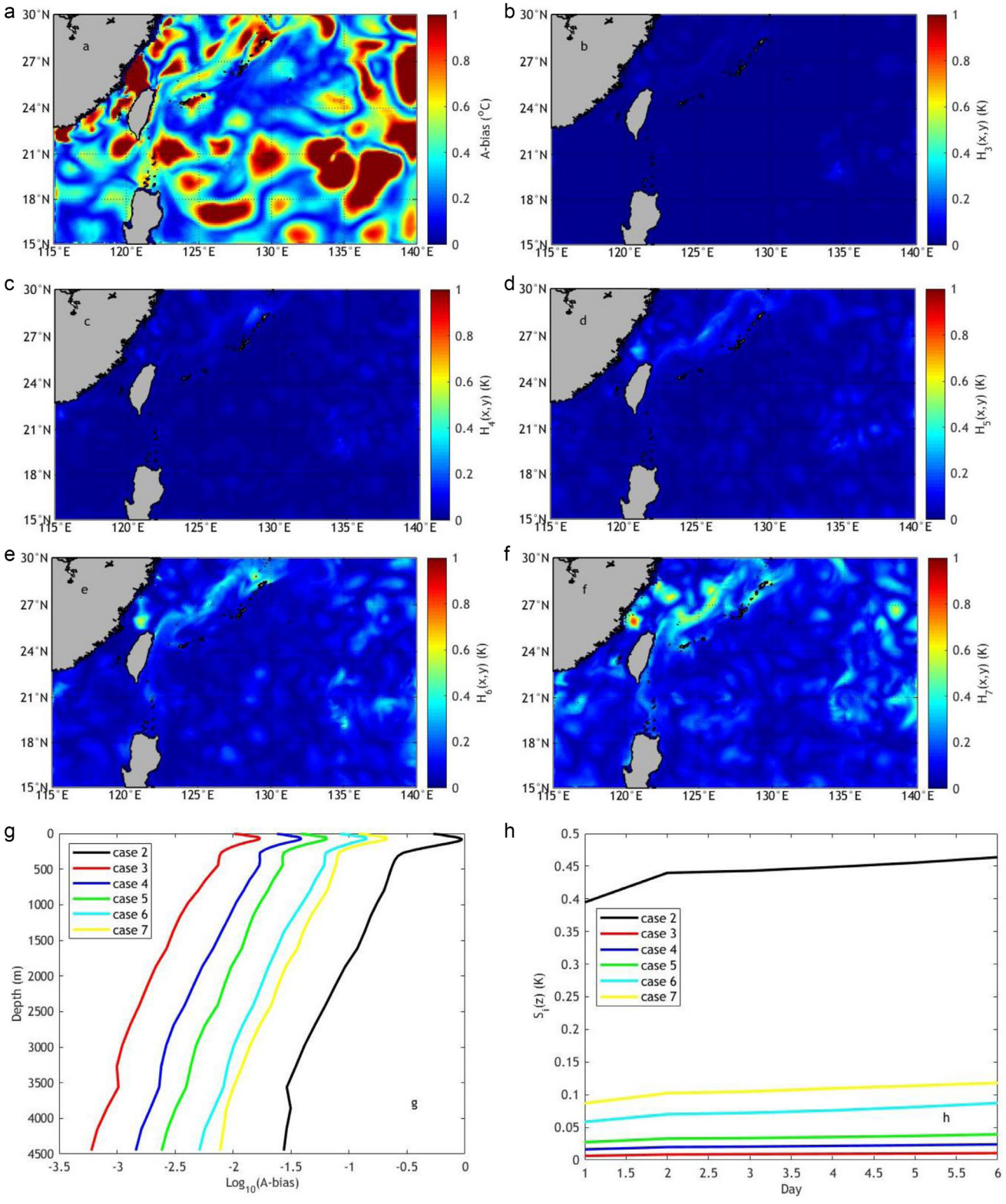

Figure 12 Evaluation of temperature outcomes of SSH assimilation cases at different levels of accuracy. Here, graphs a)–d), each presents the temporal and vertical averaged error $H_i(x,y)$ (i=2, 3, 4, 5, 6, 7) of the 3D temperature field for cases 2–7. Otherwise, graph e) and f) present the temporal and horizontal averaged error $V_i(z)$ and spatial averaged error $S_i(t)$, in which lines with different color give the results of cases 2–7, respectively.

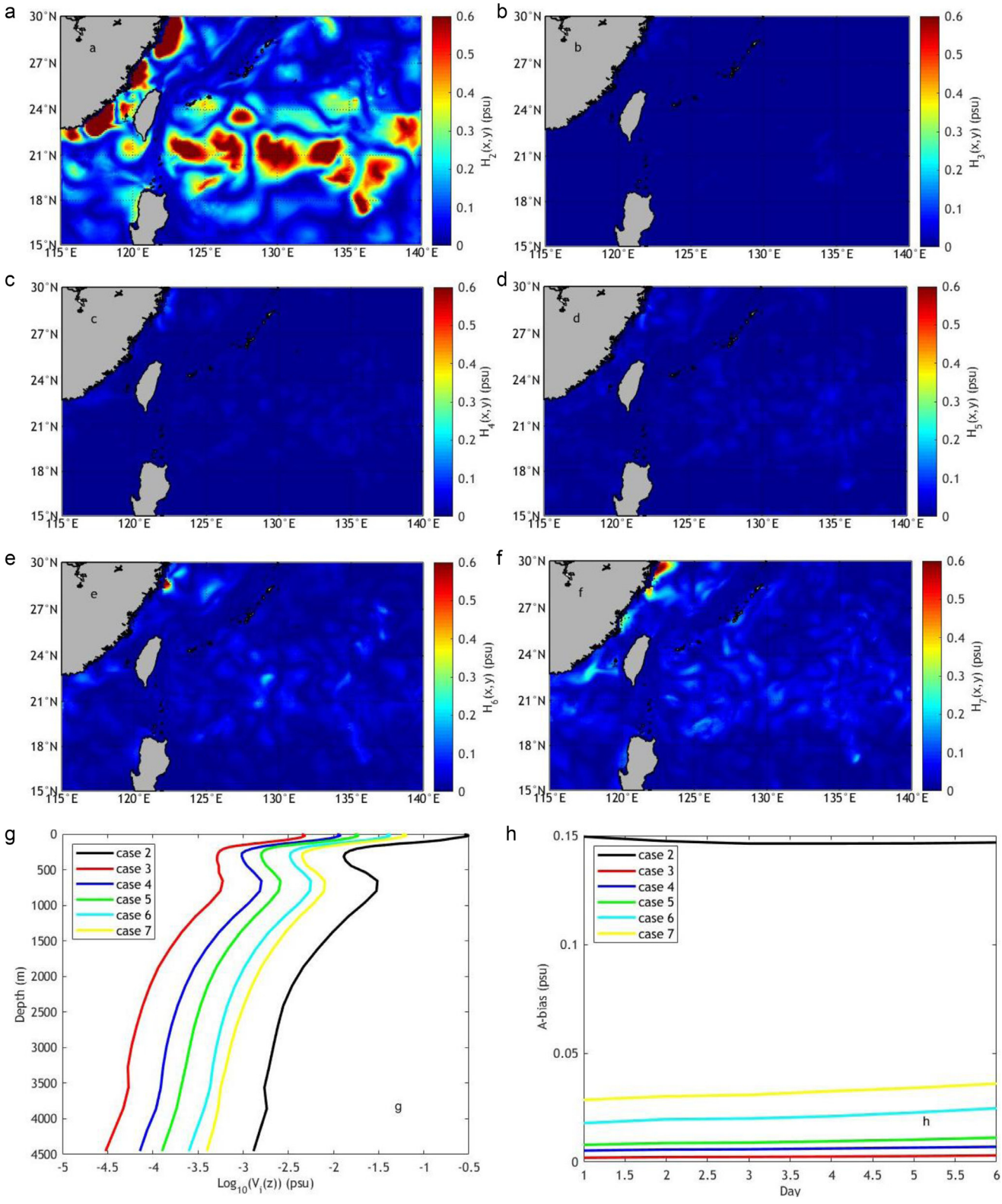

Figure 13 Evaluation of the salinity outcomes of SSH assimilation cases at different levels of accuracy. Graphs a)–h) are presented in the similar way to those in Figure 12, but for the salinity field.

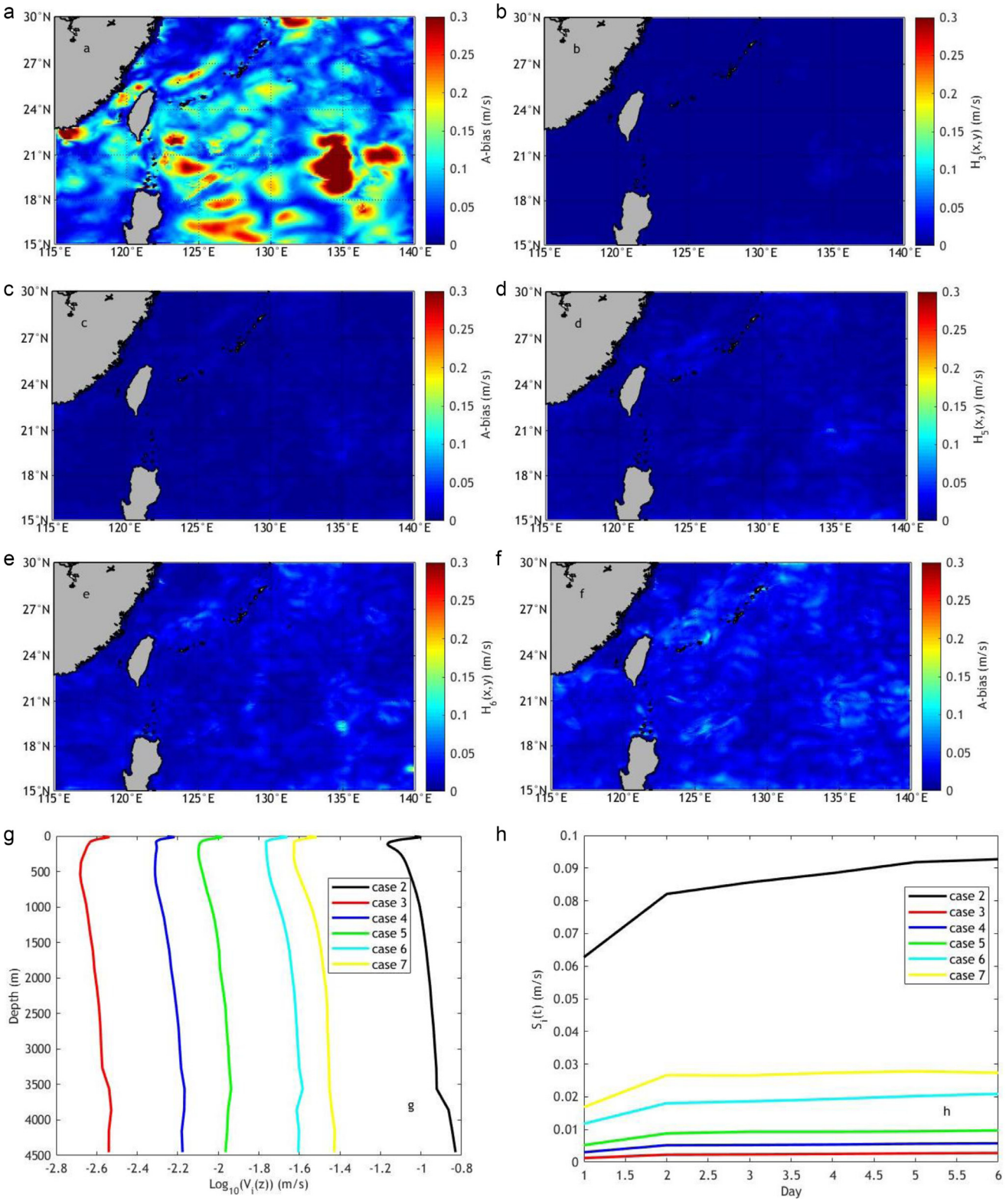

Figure 14 Evaluation of the velocity (eastward component) outcomes of SSH assimilation cases at different levels of accuracy. Graphs a)–h) are presented in the similar way to those in Figure 12, but for the 3D velocity field.

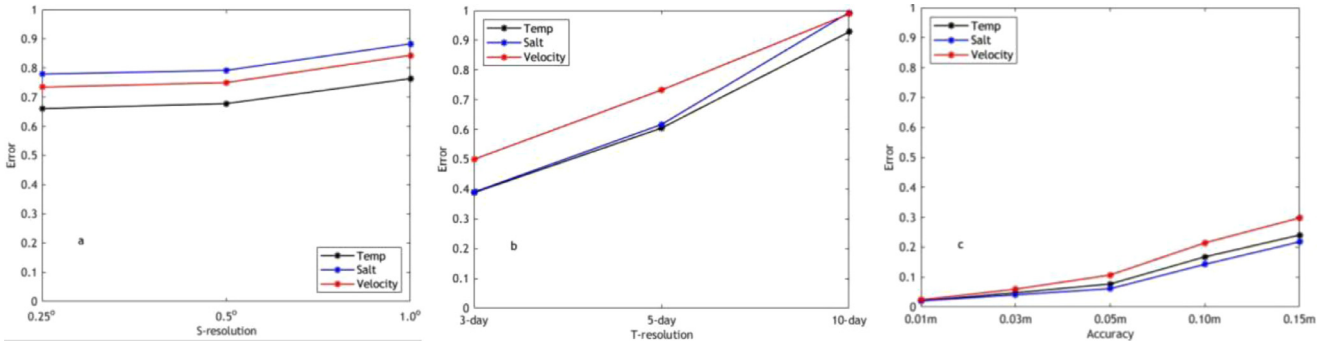

Figure 15 Normalized error statistics. Graphs a)—c) represent the results of SSH assimilation experiments using different spatial and temporal resolutions and different accuracy levels.

0, respectively. Assuming the error series were represented by e_i, then the formula for the normalization is:

$$E_i = \frac{e_i - \min(e_i)}{\max(e_i) - \min(e_i)}.$$

After that, all the errors were set between 0 and 1, i.e., $E_i \in (0, 1)$.

The normalized T-S-V errors of the three groups of experiments are shown in Figure 15. In each graph, the slope of the curves is regarded as the sensitivity to the corresponding data feature. Thus, as shown in the figure, the 3D T-S-V field was demonstrated to be the most sensitive to the temporal resolution of wide-swath SSH observations, which confirmed the above conclusion. Thus, if we would like to model the 3D ocean state by assimilating the wide-swath altimeter observations, the temporal resolution or the assimilation interval is the parameter which deserves more attention.

5. Conclusions

In this study, the impact of wide-swath altimeter observations on the construction of the oceanic 3D T-S-V field was investigated, based on ROMS and 4DVAR. Using the AVISO gridded products and the observe orbit of Jason-2, the wide-swath altimetry measurements were simulated and generated at different spatial and temporal resolutions and levels of accuracy. After that, three groups of experiments were performed to examine the impact of these features on the assimilation results. In each group, the derived ocean T-S-V fields were evaluated by the specified ideal scenario. The comparisons indicated that, the estimation of the 3D ocean state obtains an obvious enhancement when the wide-swath SSH information got assimilated, and the effect increased with better parameter choices. Besides, the estimate of the 3D T-S-V fields was demonstrated to be the most sensitive to the temporal resolution, for which the derived 3D T-S-V fields could be improved by up to 54%, and this conclusion was confirmed by analyzing the normalized errors.

The forthcoming wide-swath altimeter observations certainly have a positive effect on the estimates of the ocean 3D state. However, it is unrealistic for the design of the altimeter to hold all the optimal parameters at the same time, and thus some non-essential qualities must be sacrificed. In such situation, the sensitivity analysis could be applied to evaluate which parameter might be weakened. In the future, we would like to refine the quantitative assessments and evaluate the capacity to detect some ocean dynamical processes. Otherwise, we would also like to thoroughly investigate the potential applications and advantages of the forthcoming wide-swath altimetry observations.

Acknowledgments

The authors would like to thank the AVISO for providing the gridded multi-mission altimeter products (http://www.aviso.altimetry.fr). The study is supported by the National Key R&D Program of China under contract no. 2017YFC1405600, the National Natural Science Foundation of China under contract no. 41576176 and the Fundamental Research Funds for the Central Universities under contract no. 19CX05003A-6.

References

Amante, C., Eakins, BW., 2009. ETOPO1 arc-minute global relief model: procedures, data sources and analysis. NOAA Tech. Memo, 19 NESDIS NGDC-24, 25 pp.

Atlas, R., Hoffman, R.N., Ardizzone, J., Leidner, S.M., Jusem, J.C., Smith, D.K., Gombos, D., 2011. A cross-calibrated, multiplatform ocean surface wind velocity product for meteorological and oceanographic applications. B. Am. Meteorol. Soc. 92 (2), 157—174.

Bell, M.J., Schiller, A., Le Traon, P.Y., Smith, N.R., Dombrowsky, E., Wilmer-Becker, K., 2015. An introduction to GODAE OceanView. J. Oper. Oceanogr. 8 (S1), s2—s11.

Bonaduce, A., Benkiran, M., Remy, E., Traon, P.Y.L., Garric, G., 2018. Contribution of future wide-swath altimetry missions to ocean analysis and forecasting. Ocean Sci. 14 (6), 1405—1421.

Chaigneau, A., Gizolme, A., Grados, C., 2008. Mesoscale eddies off Peru in altimeter records: Identification algorithms and eddy spatio-temporal patterns. Prog. Oceanogr. 79 (2—4), 106—119.

Chelton, D.B., Schlax, M.G., Witter, D.L., Richman, J.G., 1990. Geosat altimeter observations of the surface circulation of the Southern Ocean. J. Geophys. Res.-Oceans 95 (C10), 17877—17903.

Cooper, M., Haines, K., 1996. Altimetric assimilation with water property conservation. J. Geophys. Res.-Oceans 101 (C1), 1059—1077.

De Mey, P., Robinson, A.R., 1987. Assimilation of altimeter eddy fields in a limited-area quasi-geostrophic model. J. Phys. Oceanogr. 17 (12), 2280—2293.

Ducet, N., Le Traon, P.Y., Reverdin, G., 2000. Global high-resolution mapping of ocean circulation from TOPEX/Poseidon and ERS-1 and -2. J. Geophys. Res.-Oceans 105 (C8), 19477—19498.

Evensen, G., Van Leeuwen, P.J., 1996. Assimilation of Geosat altimeter data for the Agulhas current using the ensemble Kalman filter with a quasigeostrophic model. Mon. Weather Rev. 124 (1), 85—96.

Fan, S., Oey, L.Y., Hamilton, P., 2004. Assimilation of drifter and satellite data in a model of the Northeastern Gulf of Mexico. Cont. Shelf Res. 24 (9), 1001—1013.

Gaspar, P., Ogor, F., Le Traon, P.Y., Zanife, O.Z., 1994. Estimating the sea state bias of the TOPEX and POSEIDON altimeters from crossover differences. J. Geophys. Res.-Oceans 99 (C12), 24981—24994.

Gaultier, L., Ubelmann, C., Fu, L.L., 2016. The challenge of using future SWOT data for oceanic field reconstruction. J. Atmos. Ocean. Tech. 33 (1), 119—126.

Hwang, P.A., Teague, W.J., Jacobs, G.A., Wang, D.W., 1998. A statistical comparison of wind speed, wave height, and wave period derived from satellite altimeters and ocean buoys in the Gulf of Mexico region. J. Geophys. Res.-Oceans 103 (C5), 10451—10468.

Kalnay, E., Kanamitsu, M., Kistler, R., Collins, W., Deaven, D., Gandin, L., Iredell, M., Saha, S., White, G., Woollen, J., Zhu, Y., Chelliah, M., Ebisuzaki, W., Higgins, W., Janowika, J., Mo, K.C., Ropelewski, C., Wang, J., Leetmaa, A., Reynolds, R., Jenne, R., Joseph, D., 1996. The NCEP/NCAR 40-year reanalysis project. B. Am. Meteorol. Soc 77 (3), 437—472.

Killworth, P.D., Dieterich, C., Le Provost, C., Oschlies, A., Willebrand, J., 2001. Assimilation of altimetric data and mean sea surface height into an eddy-permitting model of the North Atlantic. Prog. Oceanogr. 48 (2—3), 313—335.

Klein, P., Morrow, R., Samelson, R., Chelton, D., Lapeyre, G., Fu, L., Qiu, B., Ubelmann, C., Traon, P.L., Capet, X., Ponte, A., Sasaki, H., d'Ovidio, F., Farrar, T., Chapron, B., D'Asaro, E., Ferrari, R., McWilliams, J., Smith, S., Thompson, A., 2015. Mesoscale/sub-mesoscale dynamics in the upper ocean. NASA Surface Water and Ocean Topography (SWOT), http://www.aviso.altimetry.fr/fileadmin/documents/missions/Swot/WhitePaperSWOTSubmesoscale.pdf.

Koblinsky, C., Caspar, P., Lagerloef, G., 1992. Oceans and climate change: The future of spaceborne altimetry. EOS-T. Am. Geophys. Un. 73 (38) 403—403.

Korotaev, G., Oguz, T., Nikiforov, A., Koblinsky, C., 2003. Seasonal, interannual, and mesoscale variability of the Black Sea upper layer circulation derived from altimeter data. J. Geophys. Res.-Oceans 108 (C4), 16 pp.

Kurapov, A.L., Foley, D., Strub, P.T., Egbert, G.D., Allen, J.S., 2011. Variational assimilation of satellite observations in a coastal ocean model off Oregon. J. Geophys. Res.-Oceans 116 (C5), 19 pp.

Le Traon, P.Y., Rouquet, M.C., Boissier, C., 1990. Spatial scales of mesoscale variability in the North Atlantic as deduced from Geosat data. J. Geophys. Res.-Oceans 95 (C11), 20267—20285.

Le Traon, P.Y., Dibarboure, G., Jacobs, G., Martin, M., Rémy, E., Schiller, A., 2017. Use of satellite altimetry for operational oceanography. In: Stammer, D., Cazenave, A. (Eds.), Satellite altimetry over oceans and land surfaces. CRC Press, Boca Raton, 581—608.

Martin, M.J., Hines, A., Bell, M.J., 2007. Data assimilation in the FOAM operational short-range ocean forecasting system: A description of the scheme and its impact. Q. J. Roy. Meteoro. Soc. 133 (625), 981—995.

Martin-Neira, M., Mavrocordatos, C., Colzi, E., 1998. Study of a constellation of bistatic radar altimeters for mesoscale ocean applications. IEEE T. Geosci. Remote 36 (6), 1898—1904.

Matsumoto, K., Takanezawa, T., Ooe, M., 2000. Ocean tide models developed by assimilating TOPEX/POSEIDON altimeter data into hydrodynamical model: A global model and a regional model around Japan. J. Oceanogr. 56 (5), 567—581.

Mellor, G.L., Yamada, T., 1982. Development of a turbulence closure model for geophysical fluid problems. Rev. Geophys. 20 (4), 851—875.

Mellor, G.L., Ezer, T., 1991. A Gulf Stream model and an altimetry assimilation scheme. J. Geophys. Res./-Oceans 96 (C5), 8779—8795.

Miller, L., Cheney, R.E., Douglas, B.C., 1988. GEOSAT altimeter observations of Kelvin waves and the 1986—87 El Nino. Science 239 (4835), 52—54.

Moore, A.M., Arango, H.G., Broquet, G., Edwards, C., Veneziani, M., Powell, B., Foley, D., Doyle, J.D., Costa, D., Robinson, P., 2011. The Regional Ocean Modeling System (ROMS) 4-dimensional variational data assimilation systems: part II — performance and application to the California Current System. Prog. Oceanogr. 91 (1), 50—73.

Morrow, R., Birol, F., 1998. Variability in the southeast Indian Ocean from altimetry: Forcing mechanisms for the Leeuwin Current. J. Geophys. Res.-Oceans 103 (C9), 18529—18544.

Nerem, R.S., Tapley, B.D., Shum, C.K., 1990. Determination of the ocean circulation using Geosat altimetry. J. Geophys. Res.-Oceans 95 (C3), 3163—3179.

Penduff, T., Brasseur, P., Testut, C.E., Barnier, B., Verron, J., 2002. A four-year eddy-permitting assimilation of sea-surface temperature and altimetric data in the South Atlantic Ocean. J. Mar. Res. 60 (6), 805—833.

Piecuch, C.G., Ponte, R.M., 2011. Mechanisms of interannual steric sea level variability. Geophys. Res. Lett. 38 (15), 6 art. no. L15605, 6 pp.

Powell, B.S., Arango, H.G., Moore, A.M., Di Lorenzo, E., Milliff, R.F., Foley, D., 2008. 4DVAR data assimilation in the intra-Americas sea with the Regional Ocean Modeling System (ROMS). Ocean Model 23 (3—4), 130—145.

Pujol, M.I., Dibarboure, G., Le Traon, P.Y., Klein, P., 2012. Using high-resolution altimetry to observe mesoscale signals. J. Atmos. Ocean. Tech. 29 (9), 1409—1416.

Qiu, B., Chen, S., 2005. Variability of the Kuroshio Extension jet, recirculation gyre, and mesoscale eddies on decadal time scales. J. Phys. Oceanogr. 35 (11), 2090—2103.

Shchepetkin, A.F., McWilliams, J.C., 2005. The regional oceanic modeling system (ROMS): a split-explicit, free-surface, topography-following-coordinate oceanic model. Ocean Model 9 (4), 347—404.

Soto-Mardones, L., Parés-Sierra, A., Garcia, J., Durazo, R., Hormazabal, S., 2004. Analysis of the mesoscale structure in the IMECOCAL region (off Baja California) from hydrographic, ADCP and altimetry data. Deep Sea Res. Pt. II 51 (6—9), 785—798.

Strub, P.T., James, C., 2002. Altimeter-derived surface circulation in the large—scale NE Pacific Gyres.: Part 1. Seasonal variability. Prog. Oceanogr. 53 (2—4), 163—183.

Tandeo, P., Chapron, B., Ba, S., Autret, E., Fablet, R., 2014. Segmentation of mesoscale ocean surface dynamics using satellite SST and SSH observations. IEEE T. Geosci. Remote 52 (7), 4227—4235.

Traon, L.P., 1991. Time scales of mesoscale variability and their relationship with space scales in the North Atlantic. J. Mar. Res. 49 (3), 467—492.

Vélez-Belchí, P., Centurioni, L.R., Lee, D.K., Jan, S., Niiler, P.P., 2013. Eddy induced Kuroshio intrusions onto the continental shelf of the East China Sea. J. Mar. Res. 71 (1—2), 83—107.

Wang, G., Su, J., Chu, P.C., 2003. Mesoscale eddies in the South China Sea observed with altimeter data. Geophys. Res. Lett. 30 (21) 6-1—6-4.

Wang, X., Liu, P.L.F., 2006. An analysis of 2004 Sumatra earthquake fault plane mechanisms and Indian Ocean tsunami. J. Hydraul. Res. 44 (2), 147—154.

Zhou, C., Ding, X., Zhang, J., Yang, J., Ma, Q., 2018. An evaluation of sea surface height assimilation using along-track and gridded products based on the Regional Ocean Modeling System (ROMS) and the four-dimensional variational data assimilation. Acta Oceanol. Sin. 37 (9), 50—58.